

Diagnosis-guided Attack Recovery for Securing Robotic Vehicles from Sensor Deception Attacks

Pritam Dash
pdash@ece.ubc.ca

University of British Columbia, Canada

Mehdi Karimibiuki
mkarimib@ece.ubc.ca

University of British Columbia, Canada

Guanpeng Li
guanpeng-li@uiowa.edu
University of Iowa, USA

Karthik Pattabiraman
karthikp@ece.ubc.ca
University of British Columbia, Canada

ABSTRACT

Sensors are crucial for perception and autonomous operation in robotic vehicles (RV). Unfortunately, RV sensors can be compromised by physical attacks such as sensor tampering or spoofing. In this paper, we present *DeLorean*, a unified framework for attack detection, attack diagnosis, and recovering RVs from sensor deception attacks (SDA). *DeLorean* can recover RVs even from strong SDAs in which the adversary targets multiple heterogeneous sensors simultaneously. We propose a novel attack diagnosis technique that inspects the attack-induced errors under SDAs, and identifies the targeted sensors using causal analysis. *DeLorean* then uses historic state information to selectively reconstruct physical states for compromised sensors, enabling targeted attack recovery under single or multi-sensor SDAs. We evaluate *DeLorean* on four real and two simulated RVs under SDAs targeting various sensors, and we find that it successfully recovers RVs from SDAs in 93% of the cases.

CCS CONCEPTS

• **Computer systems organization** → **Robotic autonomy**; • **Security and privacy** → **Systems security**.

KEYWORDS

Cyber-Physical Systems, Resilience, Physical Attacks

ACM Reference Format:

Pritam Dash, Guanpeng Li, Mehdi Karimibiuki, and Karthik Pattabiraman. 2024. Diagnosis-guided Attack Recovery for Securing Robotic Vehicles from Sensor Deception Attacks. In *Proceedings of ACM ASIA Conference on Computer and Communications Security (AsiaCCS'24)*. ACM, New York, NY, USA, 15 pages. <https://doi.org/XXXXXXXX.XXXXXXX>

1 INTRODUCTION

Autonomous Robotic Vehicles (RV) such as drones and rovers RVs rely on their onboard sensors to perceive their physical states (e.g., position, angular orientation). Based on the physical states, specialized algorithms plan the RV's autonomous navigation in a feedback

Permission to make digital or hard copies of all or part of this work for personal or classroom use is granted without fee provided that copies are not made or distributed for profit or commercial advantage and that copies bear this notice and the full citation on the first page. Copyrights for components of this work owned by others than ACM must be honored. Abstracting with credit is permitted. To copy otherwise, or republish, to post on servers or to redistribute to lists, requires prior specific permission and/or a fee. Request permissions from permissions@acm.org.

AsiaCCS'24, July 01–05, 2024, Singapore

© 2024 Association for Computing Machinery.
ACM ISBN 978-1-4503-XXXX-X/18/06...\$15.00
<https://doi.org/XXXXXXXX.XXXXXXX>

control loop [24]. Unfortunately, attackers can feed erroneous sensor measurements to the RV through its physical channels (i.e., physical attacks), causing the RV to deviate from its course and/or crash [29, 41]. Physical attacks such as GPS spoofing have occurred in the wild on military drones [27] and marine systems [26].

We refer to physical attacks on RVs that target one or more sensors simultaneously as *Sensor Deception Attacks* (SDAs). SDAs have been demonstrated in autonomous driving systems [16, 36], and can also be extended to RVs. SDAs cannot be mitigated by traditional security techniques as they target the sensor hardware rather than the software. Further, attack detection [19, 38] is not enough, as the RV may crash after the detection [22]. Many drones have hardware fail-safe mechanisms (e.g., landing upon failure). However, activating these upon attack detection may not be safe, as the drone may land in adverse environments or fall into attackers' hands [6]. Therefore, it is important to recover RVs from SDAs.

Prior work on attack recovery from physical attacks [31, 45, 46], uses the RV's historic state information to derive safe control actions under the attack. However, these techniques assume that all the sensors in the RV are under attack (i.e., a worst-case recovery scenario) regardless of the number of sensors actually attacked. As a result, the recovery technique performs either overly conservative or overly aggressive recovery actions during the RV mission that leads to unnecessary mission disruptions and delays (shown later in the paper). This is because, under the worst-case assumptions, prior recovery techniques isolate all the sensors and use historic states to derive recovery control actions. Thus, they lack real-time sensor feedback and accurate information about the RV's current state. Attack recovery must ensure minimal deviations from the set path and ensure timely recovery without delaying critical tasks.

Furthermore, attackers can launch stealthy attacks on RVs, causing small disruptions that build up over time [20]. While techniques have been proposed to detect such stealthy attacks [22, 38], they incur a delay in detection due to the controlled nature of these attacks. As attack recovery techniques [31, 45, 46] rely on the RV's historic states information, the detection delay degrades the effectiveness of attack recovery. This is because the RV may have significantly deviated from the desired path before the stealthy attack is flagged.

The above issues arise from the lack of attack diagnosis, and a unified method to attack detection and recovery in RVs. To secure RVs from SDAs, we need to: (i) reliably identify sensors targeted by the SDA and selectively remove them from the RV's feedback control loop, and (ii) bridge the disconnect between attack detection and recovery to prevent the impact of detection delay on recovery.

In this paper, we propose *DeLorean*, a unified framework for attack detection, diagnosis, and recovery from SDAs in RVs. We propose a *graph-based probabilistic attack diagnosis technique* to identify the sensors targeted by the SDA (i.e., attack diagnosis), and integrate the diagnosis with existing attack recovery techniques [45, 46]. This eliminates the worst-case assumptions in recovery techniques and enables targeted attack recovery. Finally, we design methods to integrate existing attack detection [19, 22, 38] with recovery techniques to address the attack detection delay, which ensures safe recovery of the RV even from stealthy attacks.

DeLorean assumes there is an existing attack detection technique deployed on the RV [19, 22, 38]. After the attack detector raises an alert, *DeLorean* activates attack diagnosis to reason about the abnormalities in the RV's physical states under an SDA, identifies the sensors targeted by the attack, and selectively removes those sensors from the RV's feedback control loop. As RVs use sensor fusion to derive state estimates, it is challenging to attribute abnormalities in physical states to a specific sensor being under attack. We address this challenge by monitoring error inflation in *all* physical state estimates derived from the RV's sensors, and perform causal analysis using factor graphs [15] to identify targeted sensors. The attack diagnosis is independent of the analysis performed by the attack detection techniques [19, 22, 38]. This helps mask false positives in the attack detection, as it is unlikely for both the detection and diagnosis techniques to incur false positives simultaneously.

DeLorean also introduces an automated method to record attack-free historic state information of the RV while accounting for the attack detection delay. Based on attack diagnosis outcomes, *DeLorean* estimates the physical states corresponding to the compromised sensors using the historic state information, and incorporates the uncompromised sensor estimates to derive reliable RV state estimates despite the attack. Finally, the attack recovery technique uses these reliable state estimates to perform attack recovery.

By unifying attack detection, diagnosis, and recovery, *DeLorean* provides a targeted approach to recover RVs from both single and multi-sensor SDAs including stealthy attacks. *To the best of our knowledge, DeLorean is the first attack diagnosis-guided attack recovery technique for RVs.* Our contributions are as follows:

- Propose a graph-based probabilistic diagnosis approach to identify the RV's sensors targeted by SDAs through causal analysis, independent of the attack detection
- Propose automated methods to record attack-free historic state information, and state reconstruction strategies that enable existing attack recovery techniques [31, 45, 46] to perform targeted attack recovery under SDAs.
- Design *DeLorean*, a unified framework that integrates existing attack detection and attack recovery techniques with the proposed attack diagnosis technique, to provide diagnosis-guided attack recovery from SDAs.
- Evaluate *DeLorean* on six RVs - four real RVs and two simulated systems in a wide range of scenarios, and under SDAs targeting different numbers of sensors in the RV.

Our experimental results are as follows: (1) *DeLorean's* attack diagnosis under multi-sensor SDAs achieves a 96% true positive (TP) rate and a 5% false positive (FP) rate. (2) *DeLorean* effectively masks FPs from the attack detector, leading to a 4X reduction in gratuitous

recovery activations in contrast to three other baseline diagnosis approaches. (3) *DeLorean* successfully recovers RVs from multi-sensor SDAs in 93% of cases, resulting in over 2X reduction in the RV's deviations from the set path, and a 2.5X reduction in mission delays compared to a worst-case recovery technique. (4) *DeLorean* also mitigates stealthy attacks and achieves 100% mission success under such attacks, and (5) *DeLorean* incurs modest overheads in both runtime and memory when executed on real RVs, and is able to recover them from SDAs without incurring any crashes.

2 BACKGROUND AND THREAT MODEL

In this section, we present an RV's state estimation process. Then, we present sensor deception attacks (SDA), and the threat model.

2.1 State Estimation and Control in RVs

An RV's state estimation and control process operates in a feedback loop. It uses the sensor measurements to determine the current physical state of the vehicle, and derive actuator signals for positioning the vehicle in the next state. For example, GPS measures the RV's position, gyroscope measures angular velocity, accelerometer measures velocity and acceleration, magnetometer measures the heading direction, and barometer measures the altitude. In addition, RVs use sensor fusion techniques like Extended Kalman Filter (EKF) [34] to enhance the physical state estimations by fusing measurements from sensors with a model of the systems's dynamics. Typically, a PID (Proportional Integral Derivative) controller is used for the RV's position, velocity, and orientation control.

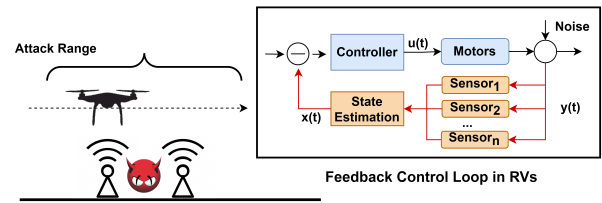


Figure 1: State Estimation and Feedback Control in RVs. SDA influencing RV's state estimation and control.

2.2 Sensor Deception Attacks

Physical attacks that manipulate sensor measurements from an external source via physical channels have been demonstrated in RVs. e.g., gyroscope measurements can be manipulated through acoustic noise injection [41, 43], and GPS measurements can be manipulated by transmitting false GPS signals [29, 37]. Such attacks are launched by injecting false data to sensor [19, 20, 23, 38].

In this paper, we consider a strong form of physical attacks against RVs - we call these *Sensor Deception Attacks* (SDA) - in which, one or more sensors in the RV are compromised simultaneously. Any possible combination of sensors can be targeted by an SDA, even up to all the sensors. An SDA is launched by injecting malicious signals to the RV's sensors. For example, an adversary can set up a fake GPS emitter, acoustic signal injectors, and magnetic signal injectors at a geographical location, and target the GPS, gyroscope, accelerometer, and magnetometer sensors simultaneously during an RV mission. Such an SDA can be debilitating for

the RVs, as it *simultaneously* corrupts the physical properties measured by different types of sensors on the RV (e.g., position, velocity, acceleration, angular velocity, heading direction etc.)

SDAs targeting multiple sensor types have been demonstrated against bare metal systems [36] and self-driving cars [16]. For drones, Nashimoto et al. [36] showed that an adversary can target gyroscope, accelerometer, and magnetometer sensors at once through acoustic and magnetic signal injection to influence state estimation even in the presence of sensor fusion (EKF). We later show that such an attack can crash a drone almost immediately.

Attackers can also exploit knowledge of an RV's attack detection strategy to launch stealthy attacks [20]. Stealthy attacks inject controlled sensor manipulations while evading detection, and can cause significant disruptions when performed over long durations [21].

2.3 Threat Model and Assumptions

We focus on physical attacks that maliciously perturb one or more of the RV's sensors' measurements. To launch the attacks, attackers can deploy signal emitters in locations of their choosing. The attacker can also manipulate any number of RV sensors during the RV mission. They can also inject sensor manipulation in a controlled manner to launch stealthy attacks. Attacks targeting RV's software components or communication channels are considered out of scope as they can be handled by existing techniques [14].

Assumptions. We make three assumptions. First, we do not consider obstacles in the RV's path, which is in line with almost all the prior work in this area [18, 22, 46]). This is because the RV's trajectory planning can be equipped with complementary obstacles or collision avoidance components if obstacles are expected in the mission [33]. Second, we assume that the RV's starting position is an attack-free zone. This is because the RV needs to gather some attack-free historical state information to enable diagnosis and recovery (details in Section 5.3). Finally, we assume that the attacker cannot control the RV's environmental conditions, e.g., wind.

3 RELATED WORK AND MOTIVATION

In this section, we first present the related work and highlight its limitations. Then, we present a motivating example for introducing attack diagnosis guided targeted attack recovery from SDAs.

3.1 Related Work

Attack Detection. Many attack detection techniques have been proposed for RVs [19, 22, 30, 38, 44], and other cyber-physical systems (CPS) [13, 17, 25] that detect attacks based on either invariants or model estimations. However, all of these techniques focus only on attack detection which, by itself, is not enough for securing RVs. All three components attack detection, diagnosis, and recovery are necessary for effectively mitigating SDAs against RVs.

Attack Recovery. We classify prior work in attack recovery on RVs into two categories as follows: (1) Model-based recovery, and (2) Checkpoint-based recovery techniques.

Model-based recovery techniques rely on a model of the RV to derive corrected sensor or actuator signals to recover RVs from attacks. For example, Software Sensor-based Recovery (SSR) [18] emulates the physical sensor signals using virtual sensors, and derives recovery control actions. Another example is PID-Piper [22],

which uses a machine learning (ML) based feed-forward controller (FFC) to derive robust actuator signals under attacks.

On the other hand, Checkpoint-based recovery techniques isolate sensors upon attack detection, and instead use the historic trustworthy states of the system to determine robust control actions and recover RVs. Kong et al. [31] use the historic states to roll forward the RV to expected states under attack. Zhang et al. use a linear programming-based recovery controller [45], and generate recovery control actions using historic states for bringing a system under attack back to a set target. In subsequent work, they proposed a linear quadratic regulator (LQR) based recovery controller [46] which improves the recovery control actions and ensures that the system remains in a safe state after recovery.

Limitations in Existing Work and Research Gap. A fundamental issue with Model-based approaches [18, 22] is that they are based on a predictive model of the RV, and hence they tolerate an error margin (approximation error) between model estimations and the RV's real behavior. The error margin is small enough under single sensor attacks to derive robust control actions for recovering the RV. However, when multiple sensors are attacked simultaneously, the model's approximation error increases. Thus, both SSR and PID-Piper are ineffective under multi-sensor attacks.

In contrast, Checkpoint-based techniques derive recovery control actions aimed at restoring the RV to a predefined state, instead of merely tolerating attack-induced manipulations. Thus, they prove superior in safeguarding RVs from attacks. However, Checkpoint-based recovery methods assume all the sensors are targeted simultaneously [31, 45, 46] and perform a worst-case recovery irrespective of the actual number of sensors targeted. We show later that the worst-case assumptions lead to overly conservative or aggressive maneuvers of the RV which result in disruptions and a failed recovery, when only a subset of sensors are attacked.

Scope of this Paper. Our goal is to bridge the gap between Model-based and Checkpoint-based techniques by enabling attack recovery methods to handle single or multi-sensor SDAs, even those that target a subset of sensors. To achieve this, we propose an attack diagnosis technique that integrates seamlessly with existing attack detection [22, 38] and recovery techniques [46]. Upon attack detection, our proposed attack diagnosis identifies the targeted sensors and isolates them from the RV's feedback control loop. Subsequently, recovery control actions are generated corresponding to the compromised sensors, eliminating the worst-case recovery assumptions when only a subset of sensors is targeted.

Further, to address attack detection delays caused by stealthy attacks which can remain undetected for a prolonged duration and impact recovery process, we design a method to determine the maximum duration a stealthy attack can remain undetected. We then synchronize attack detection, diagnosis, and recovery techniques in a unified system to prevent disruptions due to stealthy attacks.

3.2 Motivation

We performed an experiment and launched SDAs targeting a subset of the RVs sensors to highlight the gaps in the current Checkpoint-based attack recovery techniques. The details of the experimental setup are explained later (Section 5). We used the state-of-the-art Checkpoint-based recovery technique, which employs a Linear

DeLorean activates attack recovery to apply targeted recovery only for sensors that are malicious. Our framework is designed to be versatile and can integrate any Checkpoint-based recovery technique [31, 45, 46]. Note however that, none of the prior Checkpoint-based recovery techniques offer targeted attack recovery. We design a checkpointing strategy to record attack-free historic states and a state reconstruction approach that accurately represents the RV's current states under SDAs. These supporting components are designed to incorporate the outcomes of attack diagnosis, and enable Checkpoint-based techniques to perform targeted recovery actions.

DeLorean's operations are shown in Figure 3. *DeLorean* consists of three main operations as follows. (i) **Historic States Checkpointing**: *DeLorean* records trustworthy historic states from an attack-free phase of the mission in a sliding window. These historic states are used to derive recovery actions. (ii) **Attack Diagnosis**: Under an attack, *DeLorean* identifies the targeted sensors to selectively derive recovery control actions. (iii) **State Reconstruction**: *DeLorean* reconstructs the RV's states from trustworthy historical states and uncompromised sensor measurements (available when SDAs target a subset of sensors) to obtain an accurate representation of the RV's current states despite the attack induced manipulations. These reconstructed states are used by the attack recovery technique to derive the recovery control actions.

Figure 4 shows the components of *DeLorean* in RV's feedback control loop. As shown in Figure 3, *DeLorean's* first operation, *Historic State Checkpointing* is executed in the absence of attacks. ❶ A canonical attack detector uses the sensor measurements $y(t)$ to derive the RV's next physical state $x'(t)$, and compares it with the values derived by the state estimation module $x(t)$. If the residual $r = |x'(t) - x(t)|$ exceeds a predefined threshold, that indicates an attack [19, 22, 38]. Once an attack is detected, ❷ the *Diagnosis Switch* activates *DeLorean's* second operation, ❸ *Attack Diagnosis*. This step identifies the sensors targeted by the attack, and isolates the targeted sensors from the feedback control loop, preventing the attack induced sensor manipulations from propagating and causing cascading errors in the RV's feedback control loop. Based on attack diagnosis, *DeLorean's* third operation ❹ *State Reconstructor* utilizes measurements from uncompromised sensors and historical states for compromised sensors to estimate accurate state representation of the RV. Finally, ❺ the *Recovery Switch* forwards the reconstructed state estimates to the attack recovery component for deriving recovery control actions.

4.1 Attack Diagnosis

The first step in *DeLorean* is to identify the targeted sensors once an attack is detected. Attack induced sensor manipulations corrupt the RV's physical states that are estimated using the targeted sensors. For example, when the gyroscope sensor is under attack, it leads to the corruption of the RV's Euler angles (roll, pitch, yaw), and angular velocity. Table 1 shows the states to sensor mapping.

Table 1: Physical states and corresponding sensors in RVs

Sensors	GPS	Gyroscope	Accel	Barometer	Magnetometer
States	$x, y, z,$ $\dot{x}, \dot{y}, \dot{z}$	$\phi, \theta, \psi,$ $\omega_\phi, \omega_\theta, \omega_\psi$	$\ddot{x}, \ddot{y}, \ddot{z}$	z	x_m, y_m, z_m

We observe that in attack-free segments of the mission, the error between the RV's past and present states is relatively low i.e., $e_{i_t} = |state_{i_t} - state_{i_{t-1}}| \ll \delta$ and $e_{i_{t-1}} = |state_{i_{t-1}} - state_{i_{t-2}}| \ll \delta$, where $i \in PS$ (all the physical states of the RV, shown in Equation 1). However, under attack, the error e_i increases i.e., $e_i \gg \delta$ [19, 22, 38]. Therefore, our approach for attack diagnosis is to monitor the inflation in error e_i in four consecutive time steps and find the probability that the corresponding sensor is under attack given the observed errors (including both steady and non-steady state errors)

$$PS = x, y, z, \dot{x}, \dot{y}, \dot{z}, \ddot{x}, \ddot{y}, \ddot{z}, \phi, \theta, \psi, \omega_\phi, \omega_\theta, \omega_\psi, x_m, y_m, z_m \quad (1)$$

However, error inflation in the RV's physical states can also occur due to the RV's physical dynamics in the mission (e.g., mode changes), and not only due to attacks. Thus, it is important to find the root cause of the error inflation in RV's physical states. We use factor graphs (FG) to monitor the error inflation in physical state. FGs are probabilistic graphical models that allow expressing conditional relationships between variables [15]. In particular, we use FG to represent the causal relationship between the observed error e_i and find the probability that the corresponding sensor is under attack i.e., the outcome s_i . We consider binary outcomes for the sensors i.e., *malicious* (targeted by SDA) or *benign* (attack-free).

The causal relationship between e_i and s_i can be expressed as a conditional probability problem i.e., $P(s_i|e_i)$. There are two ways to calculate conditional probability: (1) Using a joint probability distribution over the observed e_i , and the probable outcomes s_i (i.e., benign or malicious sensors). However, expressing the joint probability distribution at runtime for binary outcomes will have high computation and storage overheads. Further, as the mission progresses, the time taken to calculate probabilities will increase exponentially. Therefore, this approach is not practical.

(2) Using a Bayesian approach, we can calculate $P(s_i|e_i)$ based on the values of known probabilities of $P(e_i|s_i = \text{malicious})$ and $P(e_i|s_i = \text{benign})$. To calculate $P(s_i|e_i)$, we will need to run a large number of experiments and profile the observed error e_i in the RV's physical states under attacks as well as in the absence of attacks to calculate $P(e_i|s_i = \text{malicious})$ and $P(e_i|s_i = \text{benign})$. This will also not work in our case due to two reasons: First, it is difficult to know how many observations are enough. Second, if we observe an error during inference that was not observed during profiling, the Bayesian approach will assign it a zero probability (i.e., Zero Frequency problem). Thus, even if a sensor is under attack, the Bayesian approach will wrongly conclude the sensor is benign.

In contrast to the above approaches, FGs allow fine-grained representation of the complex joint probability distribution between variables through a product of smaller probability distributions. Thus, they incur low computation and storage overheads. Further, instead of relying on profiling, FGs use functions (i.e., factor functions) to express conditional relationships. Thus, FGs can accommodate unseen observations (e_i), and do not suffer from the Zero Frequency problem. This is why we use FGs for attack diagnosis.

Figure 5 shows an example of FG-based diagnosis. The FG represents the relationships between error $E = (e_1, \dots, e_n)$ and the probable outcome $S = (s_1, \dots, s_n)$ using a bipartite graph, where e_i and s_i are observed error and outcomes of the RV's physical states (Equation 1). Factor functions $F = (f_1, \dots, f_n)$ define relationships between observed errors (e_{i-1}, e_{i_t}) and probable outcomes s_i . Using

FGs, we calculate the probability of each physical state s_i being malicious given the observed error e_i i.e., $P(s_i = \text{malicious}|e_i)$. If certain physical states are found to be malicious, we deem the corresponding sensors (Table 1) to be under attack.

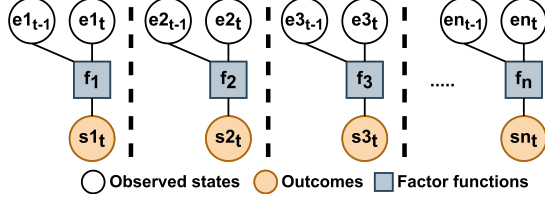


Figure 5: Factor graph for diagnosing malicious sensors under an SDA given the observed errors in RV's physical states.

Factor Graph Construction. The steps involved in constructing the FGs and using FGs for attack diagnosis are as follows.

Step 1 - Express the causal relationships between errors in RV's physical states and the probable outcome using factor functions. To express such a relationship, the first step is to determine the safe and unsafe ranges of the error e . We run attack-free missions and collect mission traces, and we observe the variation in error e . Recall that in an attack free phase, the error is low: $e + \epsilon$, where ϵ is environmental noise. We deem e to be in the safe range if $0 < e < \delta$, where $\delta = \text{median}(e) + k * \text{stdev}(e)$. The value of δ is RV-specific, and it is derived empirically (details in Section 6).

The factor functions rely on the δ values of the respective physical states to output a discrete value representing the possible outcome for each sensor (Equations 2). In particular, the factor function expresses the relations if $e_{i,t-1} > \delta$ and $e_{i,t} > \delta$, then what is the most probable outcome for the sensor (malicious or benign)? Note that we monitor errors in the past four states ($e_{i,t} = |\text{state}_t - \text{state}_{t-1}|$, $e_{i,t-1} = |\text{state}_{t-2} - \text{state}_{t-3}|$) to disregard transient error inflation and benign changes in physical dynamics in the mission.

$$f_i(e_{i,t-1}, e_{i,t}, s_{i,t}) = \begin{cases} 1, & e_{i,t} > \delta \text{ and } e_{i,t-1} > \delta \text{ and if } s_{i,t} = \text{malicious} \\ 0, & \text{otherwise} \end{cases} \quad (2)$$

Step 2 - Construct per sensor factor graphs. We repeat Step-1 and construct FGs expressing relationships between the observed errors e_i and the probable outcomes s_i for all the physical states corresponding to all the sensors of the RV. The factor functions shown in Equation 2 is used for this purpose (only the value of δ changes, which is empirically determined).

Step 3 - Perform inference on the factor graphs to diagnose the targeted sensors. We feed the physical states derived from sensor measurements to the per-sensor FGs to determine the targeted sensors. We calculate the probability of $s_{i,t} = \text{malicious}$, for all the physical states PS (Equation 1) given the observed $e_{i,t-1}, e_{i,t}$. The joint probability distribution can be factorized as:

$$P(E_t, S_t) = \prod_{i=1}^n f_i(e_{i,t}, e_{i,t-1}, s_{i,t}), \quad i \in PS \quad (3)$$

Thus, at each time t , the conditional probability is

$$P(s_{i,t} = \text{malicious}|e_{i,t}) = \prod_{i=1}^n f_i(e_{i,t}, e_{i,t-1}, s_{i,t}), \quad i \in PS \quad (4)$$

We assume that each sensor is initially equally likely to be in a benign or malicious state, so $P(s_i = \text{benign}) = 0.5$ and $P(s_i = \text{malicious}) = 0.5$. We use Maximum Likelihood Estimation (MLE) to find the likelihood of each possible outcome of s_i given the observed errors e_i . Because the observed e_i inflates under attacks, the $P(s_i = \text{malicious}) > P(s_i = \text{benign})$. We deem those states to be malicious where $P(s_{i,t} = \text{malicious}) > 0.5$, and deem the corresponding sensors (Table 1) as being under attack.

4.2 Historic States Checkpointing

When the RV is in an attack free phase, we record the sequence of physical states estimated from all the on-board sensors in a sliding window. Figure 6a shows the details. The physical states at time t are represented as $x(t)$, and the historic physical states recorded in a window are represented as HS (states shown in Equation 1).

From the start of the RV's mission, we record HS in a sliding window of length w . If no alert is raised by the attack detector, we save the HS recorded in window w_i and proceed recording states in the next window w_{i+1} as shown in Figure 6a. At the end of window w_{i+1} , we discard the HS recorded in the previous window w_i . However, if we detect an attack as shown in Figure 6b, we stop the recording, and discard the states recorded in the current window w_i as these may be corrupted by the attack. We use the HS recorded in the previous window w_{i-1} for state reconstruction and recovery. These HS are attack-free as no alert was raised by the attack detector in window w_{i-1} .

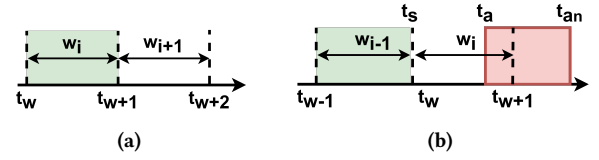


Figure 6: (a) Recording historic physical states in a sliding window. (b) Ensuring historic states are attack-free.

Another challenge is that sensors in RVs are sampled at different rates e.g., the sampling rate for gyroscope is 400 Hz, whereas, the sampling rate for Barometer is 100 Hz. It is important to align the data streams when recording the historic states. To address this problem, we select a single target frequency for recording the HS , which is the highest sampling rate of all the sensors. We then align the low frequency streams with the high frequency streams by inserting additional data points in the low frequency stream to match the sample points in the high frequency streams. In particular, we duplicate the last data point in the low frequency streams based on the ranges of the sample points of the high frequency streams.

Recovery under Stealthy Attacks. However, it is possible for an attack to be stealthy and span multiple sliding windows [20], in which case, it will be challenging to ensure an attack-free HS for recovery. Such stealthy attacks can inject seemingly benign and controlled bias in the sensor measurements over a long time, thereby evading detection, and causing disruption in the RV's mission. Many attack detection techniques such as Savior [38] and PID-Piper [22] detect stealthy attacks using cumulative sum statistics (CUSUM). However, there is necessarily a delay in attack

detection i.e., the time interval between the onset of the stealthy attack and the time when the attack detector raises an alert. Due to the detection delay, *DeLorean* might record corrupted *HS* for recovery, which it incorrectly deemed safe as no alarms were raised by the attack detector. Therefore, to handle stealthy attacks, we empirically choose the window length to be large enough so that stealthy attacks can be detected within a single sliding window.

4.3 State Reconstruction

After identifying targeted sensors through attack diagnosis, we reconstruct the RV's state vector represented as $X'(t)$. The goal of state reconstruction is to ensure accurate current state representation for the sensors affected by SDAs (referred to as $x_r(t)$), while preserving the state derived from sensors that remained unaffected by the attack at the time when recovery is activated. Furthermore, the state reconstruction process plays a key role in enabling targeted attack recovery as it facilitates real-time sensor feedback (if available i.e., when SDAs target only a subset of the sensors).

We use the Extended Kalman Filter (EKF) [34] to estimate $x_r(t)$ using the latest trustworthy historic states under SDAs. The EKF estimator is constructed offline using the RV's non-linear system dynamics (Appendix A.2). The parameters of the non-linear equations are learned using a dataset of control actions and sensor measurements. We collect the data using our subject RVs (Section 5). We learn an approximate model of the RV $f(x_t, u_t)$ through system identification [10]. The model parameters are optimized using the least squared error approach, i.e., minimize squared error between the model's estimations and the observed values.

Taking the scenarios in Figure 6b as an example, the latest trustworthy states x_{t_s} are recorded at time t_s . The RV's states evolve over time as per its system's dynamics [34]. For example, at time t_{s+1} the RV's states are calculated as $x_r(t_{s+1}) = f(x_{t_s}, u_{t_s}) + v_{t_s}$, where u_{t_s} and v_{t_s} are control inputs and process noise respectively. The above step is iteratively performed for each time step between t_s and t_a (i.e., $t_{s+1}, t_{s+2}, \dots, t_a$) to estimate RV's states $x_r(t_a)$. The EKF relies on system's dynamics and trustworthy historic states instead of compromised sensor measurements.

We reconstruct the RV's state vector at t_a when recovery is activated as follows. For sensors that remain uncompromised under SDA, we use the states derived from the corresponding sensors, these states are represented as $x_c(t_a) = x_{c_1}, \dots, x_{c_n}$. We use the trustworthy historic states to estimate states corresponding to the sensors that are targeted by the SDA, these states are represented as $x_r(t_a) = x_{r_1}, \dots, x_{r_n}$. We reconstruct RV's state vector by selectively combining the states derived from uncompromised sensors and estimated states for the compromised sensors as $X'(t_a) = [x_c(t_a), x_r(t_a)]$ to obtain accurate current state representations. $X'(t_a)$ is the initial system state of recovery.

5 EXPERIMENTAL SETUP AND PARAMETERS

In this section, we present our experimental setup, metrics, and attack parameters for evaluating *DeLorean*. We then present *DeLorean*'s parameters derived from our experiments¹.

Subject RVs: To evaluate *DeLorean*, we use six RV systems. Four of these are real RVs. These are shown in Figure 7 (from the left) (1) Pixhawk based DIY drone [35] (Pixhawk drone), (2) Tarot 650 drone [11] (Tarot drone) (3) Aion R1 ground rover [2] (Aion rover), and (4) Sky Viper Journey drone [9] (Sky-viper drone). The first three RVs are based on the Pixhawk platform [35]. The Sky-viper drone is based on an STM32 processor. These RVs are all equipped with at least one of the following five sensors: GPS, gyroscope, accelerometer, barometer and magnetometer, but each RV has different numbers of individual sensors (Table 2). The other two RV systems are simulated RVs, (4) Ardupilot's quadcopter (ArduCopter), and (5) Ardupilot's ground rover [4] (ArduRover). We use the APM SITL [4], and Gazebo [7] platforms for simulations.



Figure 7: Real RV Systems (a) Pixhawk drone, (b) Tarot drone, (c) Aion Rover, (d) Sky Viper drone.

RV Missions: We run a diverse set of 340 missions with varying mission duration, and mission distances. A mission is an autonomous navigation path of the RV, including a starting point, intermediate waypoints, and a designated endpoint. We simulate a wind flow between 0-10 m/s to vary the environmental conditions. The mission emulates various real-world RV missions: (1) a last mile delivery drone [28] (straight line path, polygonal path), (2) drones used for surveillance or agriculture [1] (circular or polygonal path), and (3) rovers deployed in warehouse management [3] (polygonal paths). Appendix A.4 discusses the RV mission paths in depth.

Table 2: Subject RVs in Evaluation, Number of Sensors, Attack parameters. P: Pixhawk drone, T: Tarot drone, S: Sky-viper drone, AC: ArduCopter, R1: R1 rover, AR: ArduRover

Sensor Type	Number of Sensors						Bias Values	Max Range
	P	T	S	AC	R1	AR		
GPS	1	1	1	1	1	1	5-50m	200
Gyroscope	3	3	1	3	3	3	0.5-9.47 rad	100
Accelerometer	3	3	1	3	3	3	0.5-6.2 rad/s ²	26
Magnetometer	3	3	1	1	3	1	180 deg	-
Barometer	1	2	1	1	1	1	0.1 kPa	-

5.1 Comparison with Prior Work

Attack Recovery: We quantitatively compare *DeLorean* with three prior attack recovery techniques discussed earlier namely SSR [18], PID-Piper [22], and LQR-O [46]. Recall that LQR-O refers to the recovery technique proposed by Zhang et al. which performs worst-case recovery irrespective of the number of sensors targeted under SDA. We collected mission traces of RVs, including both training and testing sets, and assessed the efficacy of existing recovery techniques by reproducing their effectiveness as reported in the respective papers. Subsequently, we evaluate all three recovery techniques under SDAs to observe their effectiveness under multi-sensor SDAs targeting different numbers of sensors in the RV.

¹We have made our code and data publicly available at <https://github.com/DependableSystemsLab/DeLorean>

Attack Diagnosis: There is no prior work that addresses attack diagnosis in RVs (to the best of our knowledge). We extend two existing model-based attack detection techniques namely Savior [38] and PID-Piper [22], to serve as a potential solution for attack diagnosis. Model-based attack detectors estimate RV's physical states and compare them with the physical states derived from sensors to compute a residue $r = |Model_{states} - Sensor_{states}|$. Traditionally, these attack detectors analyze residues in just one or two of the RV's physical states, sufficient for flagging an attack. We extend the concept of residual analysis (RA) to monitor all the physical states in RVs for attack diagnosis. Furthermore, RV's are equipped with EKF that estimates the RV's physical states, and uses sensor measurements to enhance state estimations (Section 2.1). EKF estimations can be potentially used for attack detection and attack diagnosis by performing residual analysis to monitor EKF estimations and sensor states. When a residue for a specific state exceeds the threshold, the corresponding sensor is deemed to be under attack (Table 1 shows states to sensor mapping). We compare *DeLorean* with the above three baseline RA-based diagnosis techniques.

5.2 Metrics

Recovery Success Metric: As in our prior work [22], we consider a mission to be successful, if upon completion, the total deviation from the original destination is *less than 10m*. Most GPS sensors used in commodity RVs have an offset of 5 meters [40]. We consider 2X of the GPS offset as our threshold i.e., 5m offset from the RV's position, and 5m offset from the destination. This 10m threshold is indistinguishable from the standard GPS error [40]. We consider the mission to be unsuccessful if the RV crashes (physically damaged) or stalls (freezes or stops moving towards the destination).

Recovery Stability Metric: To measure the stability of the RV during recovery we use the Root Mean Square Deviation (RMSD) of the RV's attitude i.e., roll, pitch, and yaw angles. This metric quantifies the average magnitude of deviations in a recovery-activated mission compared to an attack-free (ground truth) mission on the same trajectory. We calculate RMSD using the same method as Root Mean Square Error, as depicted in Equation 5. As minor attitude deviations between two RV missions even on the same trajectory is expected, we account for these expected deviations by normalizing RMSD with respect to the minimum and maximum expected deviations for an RV on a specific trajectory. (details in Appendix A.5).

$$RMSD = \sqrt{\frac{1}{n} \sum_{i=1}^n (x_{recovery} - x_{groundTruth})^2} \quad (5)$$

Mission Delay due to Recovery: We compare the mission completion time between a recovery activated mission with an attack-free ground truth mission on the same trajectory. This allows us to calculate potential mission delays resulting from the recovery process. Given that, there might be minor variations in the mission completion times even in the same trajectory, we normalize the mission delay using baseline mission completion time $T_{baseline}$ for an RV on a given trajectory (details in Appendix A.5). The percentage mission delay is calculated as shown in Equation 6.

$$PMD = \frac{T_{recovery} - T_{groundTruth}}{T_{baseline}} \times 100 \quad (6)$$

Runtime Overheads: We measure the overheads in CPU times, battery consumption, and memory incurred by the RV due to *DeLorean*. As the overheads in simulated RVs depend on the simulation platform, we report the overheads only for the real RVs. For CPU overheads, we measure the CPU times incurred by the autopilot modules with and without *DeLorean*. During the recovery process, the RV executes the prescribed recovery control actions in place of the actions generated by the PID controller. As a result, the RV's motor rotation rates increase. We call this operational overhead. We estimate the battery overhead of *DeLorean* based on both the CPU overhead and the operational overhead. Finally, we estimate the memory overhead for storing the historic states on the RV corresponding to all the RV's sensors for targeted attack recovery.

5.3 Attack Parameters

Attacks: As we did not have access to special equipment (e.g., noise emitter, sound source, amplifier, etc.) for mounting physical attacks, we emulated the attacks through targeted software modifications, similar to what most prior work has done [18, 19, 22, 38]. Our attack code interfaces with the sensor libraries in the RV, and manipulates sensor measurements by adding a bias to them (i.e., false data). When an attack command is initiated, the bias values are automatically added to the raw sensor measurements. We derive the attack parameters i.e., bias values and attack range to mimic realistic physical attacks via software as closely as possible.

Sensor Bias Values: We use variable bias values for each sensor within the allowable limit to cause mission delays, instability, and even mission failure. We derive bias values as per the respective sensor specifications. Table 2 shows the bias values used for each sensor. For example, the update frequency of the GPS module used in many industrial and commodity RVs is 0.1s, and the operational limit in its velocity is 500 m/s [12]. Therefore, the maximum hopping distance of the GPS receiver is 50m (update frequency \times maximum velocity). Thus, for GPS, we set the bias value to be between 5-50m, which is the operating limit of the GPS sensor.

Attack Range: We derive the maximum attack range based on prior work that performed the respective attacks through signal injection [36, 37, 42]. We extrapolate their results considering the largest available signal source and amplifier to derive the maximum attack range for each sensor. We found that the optimal attack range for individual sensors is within 26 – 200m. Of all the sensors, the GPS has the maximum attack range [42] of 200m. *Thus, we select 200m as the attack range for each instance of SDAs in our experiments i.e., we assume that attackers can manipulate all or any subset of the RV's sensors in a 200m range.* This is a stronger assumption than that made in all the prior work in the area [41, 43].

5.4 DeLorean Modules and Parameters

Attack Detector: As mentioned, *DeLorean* relies on an attack detection technique, and it provides attack diagnosis and targeted attack recovery after the attack is detected. For attack detection, we use our prior work, PID-Piper's attack detection module [8], as it represents the state-of-the-art and has a high detection rate. We do not measure the effectiveness of the attack detector (true positives, and false positives) - this is reported in our prior work [22].

Table 3: δ values for per sensor factor graphs in each subject RVs. position (x, y, z) in meters (m), velocity $(\dot{x}, \dot{y}, \dot{z})$ in m/s , acceleration $(\ddot{x}, \ddot{y}, \ddot{z})$ in m/s^2 , Euler angles (ϕ, θ, ψ) in degrees, angular velocities $(\omega_\phi, \omega_\theta, \omega_\psi)$ in rad/s, magnetic fields (x_m, y_m, z_m) in Gauss(G), Altitude is in meters. (values rounded up to 1st decimal place). WS: Window size for historic states recording.

RV Type	GPS						Accel			Gyroscope				Mag			Baro	WS	CPU	Battery	Memory		
	x	y	z	\dot{x}	\dot{y}	\dot{z}	\ddot{x}	\ddot{y}	\ddot{z}	ϕ	θ	ψ	$\dot{\phi}$	$\dot{\theta}$	$\dot{\psi}$	x_m	y_m					z_m	Alt
Pixhawk	3.4	5.1	5.2	2.1	10.2	5.5	6.5	4.2	10.5	12.2	9.8	45.5	11.5	13.8	1.1	0.6	0.3	0.5	0.2	15.5s	8.8%	22%	0.47MB
Tarrot	5.5	3.4	6.5	1.8	8.1	4.2	8.1	7.7	9.2	10.2	9.5	38.9	10.2	10.6	1.1	0.3	0.3	0.4	0.2	15s	6.7%	18.75%	0.45MB
Sky-Viper	4.6	3.0	4.1	1.7	7.8	3.1	5.5	4.2	5.6	13.3	11.2	58.5	14.5	16.1	1.5	0.6	0.6	0.5	0.2	17s	9.2%	20%	0.52MB
AionR1	2.7	2.5	-	1.9	6.4	-	3.3	3.5	-	-	-	45.2	-	-	2.2	-	-	-	-	18.5s	5.5%	14.4%	0.56MB
ArduCopter	3.7	3.3	4.5	2.1	9.3	4.2	5.2	6.5	7.1	9.7	9.5	36.2	9.5	11.2	1.1	0.3	0.2	0.5	0.1	15.5s	-	-	-
ArduRover	4.2	4.1	-	2.4	7.3	-	3.5	3.9	-	-	-	38.5	-	-	1.8	-	-	-	-	17s	-	-	-

Attack Diagnosis: The attack diagnosis module monitors the error e between the past and present states of the RV. Recall that in the attack-free phase, e remains within $0 - \delta$. This holds true regardless of whether the RV is in a steady or non-steady state. We use the standard deviation method to derive the value of δ i.e., $\delta = \text{median}(e) + k * \text{stdev}(e)$ i.e., if the error e is more than k standard deviations away from the mean, it is likely to be an outlier (due to the attack) [39]. We collect attack-free RV mission traces (on both simulated and real RVs with diverse mission trajectories), and empirically determine that $k = 3$ ensures $0 < e < \delta$ in the attack-free phase of the mission. We run between 15-25 attack-free missions for each RV to derive the δ values, and we validated δ values (i.e., $e \in 0 - \delta$) by running another 15 missions.

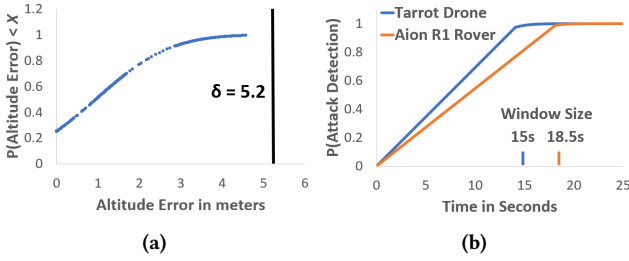


Figure 8: (a) CDF of error distribution in the Pixhawk drone. $k = 3$ ensures $0 < e < \delta$ in attack-free phase. (b) CDF of the likelihood of stealthy attack detection. Window size of 15s (Tarrot) and 18.5s (Aion A1) ensures 100% attack detection.

Figure 8a shows an example of δ for position error in the Pixhawk drone. The figure shows the Cumulative Distribution Function (CDF) of error e as a function of the probability that the physical states errors will take a value less than δ . With $k=3$, we obtain the δ value for z -axis position error as 5.2. As shown in Figure 8a, in the attack-free phase, the error e always remains under the δ . Table 3 shows the δ values for all the physical states of our subject RVs.

Attack Recovery under Stealthy Attacks: Recall that we prevent disruptions due to stealthy attacks by setting the window size for recording historic states to be large enough that stealthy attacks can be detected in a single sliding window (Section 4.2). The key question is what is the maximum duration that the attacker can cause disruptions in the RV mission by launching stealthy attacks while evading detection. Subsequently, we can set an appropriate window size for the effective detection of stealthy attacks. Therefore, to find the appropriate window size, we launched two kinds of

stealthy attacks by injecting persistent bias: (1) targeting all the sensors simultaneously, (2) targeting each sensor individually.

Note that the above stealthy attacks were launched on all of our subject RVs, in the presence of PID-Piper’s attack detector [22] that uses CUSUM to detect stealthy attacks [20]. We find that when all the sensors are manipulated persistently, the stealthy attack is detected in under 3.3s. However, when the attack targets individual sensors, the stealthy attacks against GPS remain undetected for the maximum duration i.e., around 15 – 18s.

We determine the window size for each RV to be larger than the duration of a stealthy attack that targets GPS. Figure 8b shows a CDF that depicts for how long a stealthy attack targeting GPS can evade detection as the mission progresses. 100% attack detection rate is achieved for Tarrot drone at 15s, and for Aion R1 rover at 18.5s. Thus, we select window sizes of 15s and 18.5s for the respective RVs, as the likelihood of detecting stealthy attacks in that window is near 100%. Table 2 shows the window sizes for all RVs derived in the same manner.

6 RESULTS

We first evaluate *DeLorean’s* attack diagnosis under SDAs in a simulated RV. Then, we evaluate *DeLorean’s* targeted attack recovery and compare it with other techniques under SDAs in the simulated RVs. We then study the significance of attack diagnosis under multi-sensor SDAs, followed by *DeLorean’s* attack diagnosis and recovery in real RVs. We also study *DeLorean’s* effectiveness under stealthy attacks. Finally, we present the overheads incurred by *DeLorean*.

6.1 Effectiveness of *DeLorean’s* Attack Diagnosis

In this section, we evaluate the effectiveness of *DeLorean’s* attack diagnosis by measuring the true positives (TP) and false positives (FP). TP is the fraction of times attack diagnosis correctly identified the sensors targeted by SDA. FP is the fraction of times attack diagnosis falsely identified sensors as attacked even in the absence of an attack. because no prior work has addressed attack diagnosis, we extended the residual analysis in existing attack detection techniques namely Savior [38], PID-Piper [22], and EKF [34], for attack diagnosis. We compare *DeLorean’s* diagnosis that uses factor graphs with techniques that use residual analysis (RA-based diagnosis).

We run 100 missions using simulated RVs and launched SDAs targeting up to $n - 1$ sensors of the RV. We launched the same attacks for all the diagnosis techniques to compare them. Table 4 shows the results. We find that, Savior, PID-Piper, and EKF based diagnosis techniques achieve on average 60%, 56%, and 62.5% TPs respectively. In contrast, *DeLorean’s* diagnosis correctly identified

the targeted sensors in 95% of the cases (on average). This is because *DeLorean* attributes manipulations in the RV's physical states to a sensor being under attack, by performing causal analysis using factor graphs. In contrast, the RA-based techniques perform a naive attack diagnosis by simply comparing the residuals against a threshold, thus failing to achieve a high diagnosis TP rate. Thus, *DeLorean's* diagnosis resulted in 40 to 50% higher TPs rate on average than RA-based diagnosis methods (Table 4). When SDAs targeting all the sensors were launched, all the techniques including *DeLorean* achieve a high diagnosis TP rate.

False Positives and Gratuitous Recovery Activation. Note that a false alarm in detection leads to an FP in attack diagnosis, and eventually results in gratuitous recovery activation. During gratuitous recovery, the attack recovery technique generates unnecessary recovery control actions, causing needless maneuvers that result in mission disruptions and delays. We evaluate *DeLorean's* FPs in the absence of attacks to assess its gratuitous recovery activations.

Attack detection techniques raise false alarms when exposed to environmental disturbances such as wind. To measure FPs in attack diagnosis, we induce false alarms in attack detectors by simulating wind conditions. It is important to strike a balance between the attack detection accuracy and induced false alarms, and not overwhelm the attack detector with an excessive number of false alarms. Thus, we simulated a modest wind speed of 15 km/h [5].

Table 4: *DeLorean's* attack diagnosis compared with residual analysis-based diagnosis of Savior, PID-Piper, and EKF. Values are in Percentage.

Diagnosis TPs number of sensors targeted by SDA	Savior RA	PID-Piper RA	EKF RA	<i>DeLorean</i>
1	65	65	75	100
2	55	50	60	100
3	50	50	55	90
4	70	60	60	90
Average	60	56	62.5	95
FPs (no attack)	20	15	20	5

We run 20 missions in Arducopter for each technique, activating diagnosis when attack detectors raised false alarms. Table 4 shows the FPs in each technique. The corresponding attack detectors of each RA-based diagnosis technique - Savior, PID-Piper, and EKF reported false alarms in 20%, 15%, and 20% of the cases respectively. As RA-based diagnosis methods rely on attack detectors' state estimations they also incurred 15-20% FPs. In contrast, *DeLorean* masked 15% false alarms from the attack detector and incurred only 5% FPs i.e., 4X lower FPs than other diagnosis techniques.

The RA-based diagnosis techniques resulted in significantly higher FPs because they monitor the physical states' error only in the last step, and hence fail to account for the benign deviations in RV's physical states. In contrast, *DeLorean's* diagnosis monitors the sequence of errors in four previous steps (this is inherent to the FG approach, see Figure 5). Thus, FG captures the causality of manipulations in RV's physical states to infer if the corresponding sensor is under attack, and achieves both high TPs and low FPs. Furthermore, RA-based diagnosis relies on the attack detector's response, false alarms in detection propagate as FPs in diagnosis.

DeLorean performs attack diagnosis independently, allowing it to mask FPs triggered during attack detection.

The FPs in attack diagnosis resulted in gratuitous recovery activation. We find that the gratuitous recovery operations due to FPs in RA-based diagnosis resulted in RMSD of 0.095 and mission delays of more than 10% (on average). In contrast *DeLorean* incurred almost negligible RMSD of 0.0045 which resulted in $\approx 1\%$ mission delays. Thus, *DeLorean* achieves a significant reduction of 4X in gratuitous recovery activation and prevents unnecessary mission disruptions.

6.2 Effectiveness of *DeLorean's* Attack Recovery

We compare *DeLorean* with SSR, PID-Piper, and LQR-O in recovering from the SDAs on the simulated RVs. We launched 100 missions for each simulated RV protected with SSR, PID-Piper, LQR-O, and *DeLorean* respectively. We mounted the same SDAs for all four techniques varying the number of sensor types targeted from 1 up to 5 (all sensors). Note that when we say a sensor is attacked, we mean that *all* the sensors of that type are attacked in the SDA.

Table 5: *DeLorean's* recovery outcomes compared with SSR, PID-Piper, and LQR-O as a function of the number of sensors attacked. MS: Mission Success, values are in percentages.

# of sensors targeted	SSR		PID-Piper		LQR-O		DeLorean	
	Crash	MS	Crash	MS	Crash	MS	Crash	MS
1	20	64	0	100	0	90	0	100
2	56	20	64	20	0	84	0	100
3	100	0	100	0	0	84	0	100
4	100	0	100	0	4	82	4	88
5	100	0	100	0	4	82	4	82

Table 5 shows the mission outcomes of *DeLorean*, SSR, PID-Piper, and LQR-O under single and multi-sensor SDAs. From the table, SSR has a mission success rate of 64% for single sensor attacks. However, for attacks targeting two sensors, its mission success rate drops to 20% with a crash rate of 56%. PID-Piper, on the other hand, is 100% effective when only a single sensor is targeted. However, its mission success rate also drops to 20%, and its crash rate increases to 64% when two sensors are attacked. Furthermore, when 3 or more sensors are attacked, both SSR and PID-Piper incurred a 100% crash rate (0% success). Thus, *Model-based recovery techniques SSR and PID-Piper incur crashes and mission failures* for multi-sensor SDAs, and had average mission success rates of 17% and 24% respectively.

On the other hand, LQR-O has an average mission success rate of 86% with no crashes when 1 to 3 sensors are under attack. However, when 4 or more sensors are under attack, LQR-O's average recovery success drops to 82%. Because we inject variable sensor bias within the allowable range, When 4 or more sensors are targeted simultaneously, the SDA triggers aggressive deviations from the intended path influenced by the injected bias values. This makes it challenging for LQR-O to derive safe recovery control actions.

In contrast, *DeLorean* achieves 100% mission success rate when fewer than 3 sensors are attacked, and *no crashes*. When 4 or more sensors are targeted, *DeLorean* also achieves 85% mission success and 4% crash rate (same as LQR-O). *DeLorean* achieves 94% mission success rate on average across all sensor numbers, which is $\approx 4X$ higher than the mission success rates of SSR, and PID-Piper, and 10% point increase compared to LQR-O. Thus, *DeLorean* is more resilient to multi-sensor SDAs than prior techniques.

6.3 Need for Attack Diagnosis

To understand if attack diagnosis is needed for recovery from SDAs, we compare *DeLorean*'s diagnosis guided targeted attack recovery with LQR-O under SDAs targeting various numbers of sensors. Note that LQR-O assumes a worst-case recovery scenario and applies recovery operations corresponding to all the sensors irrespective of the number of sensors targeted by an SDA.

In this experiment, we perform 100 missions each for *DeLorean* and LQR-O in simulated RVs, and launch SDAs targeting 1 to 5 sensors in each mission (all combinations). In addition to mission success rate and crash rate, we measure Root Mean Squared Deviation (RMSD), and Mission Delay (MD). RMSD provides a measure of the stability of the recovery process, and MD shows the impact of recovery on the expected mission duration. Lower RMSD and MD signifies the recovery has insignificant impact on the RV mission.

Table 6: Comparison between *DeLorean* and LQR-O (without diagnosis) under SDAs. RMSD: Root Mean Squared Deviation, MD: Mission Delay (shown as the percentage increase in mission duration), MS: Mission Success Rate.

sensors targeted	LQR-O				<i>DeLorean</i>			
	RMSD	MD	Crash	MS	RMSD	MD	Crash	MS
1	0.6259	14.5	0	90	0.1236	2.41	0	100
2	0.6319	14.66	0	84	0.1552	3.66	0	100
3	0.6414	14.46	0	84	0.2733	7.75	0	100
4	0.6383	12.41	4	82	0.5784	10.31	4	88
5	0.6603	12.58	4	82	0.6603	12.58	4	82

Table 6 shows the comparison between *DeLorean* and LQR-O. As we have already discussed the mission success and crash rates for both techniques in Section 6.2, we do not repeat them here. We find that the RMSD values of LQR-O do not vary much across SDAs that target varying numbers of sensors. In comparison, *DeLorean* has 2.2X lower RMSD (on average) than LQR-O when SDAs target a subset of the RV's sensors. Furthermore, when up to 3 sensors are targeted, *DeLorean*'s recovery incurs 2X to 5X less RMSD compared to LQR-O. This is because LQR-O applies the worst-case recovery strategy in all cases. Such recovery strategy results in LQR-O applying aggressive maneuvers when a subset of sensors is targeted. Unsurprisingly, both *DeLorean* and LQR-O have the same RMSD values when all the sensors are targeted as both techniques perform the same recovery operations in such a situation. Thus, *attack diagnosis-guided attack recovery as done in DeLorean ensures minimal deviations under SDA targeting any combination of sensors.*

Furthermore, we find that LQR-O recovery on average, incurs 2.5X higher mission delay than *DeLorean* when the SDA targets only a subset of the sensors. Recall that LQR-O recovery results in higher deviations from the trajectory compared to *DeLorean*, consequently LQR-O requires more time to restore the RV to its intended path. Further, as shown in Table 6, LQR-O's mission delays are consistent for attacks targeting varying numbers of sensors. On the other hand, *DeLorean*'s mission delays for attacks targeting less than 3 sensors are significantly lower than that of LQR-O. When a single sensor is targeted LQR-O's recovery increases the expected mission duration by 14.5%. In contrast, *DeLorean* increases the mission duration only by 2.4%. However, for attacks targeting 4 or 5 sensors simultaneously *DeLorean* incurs similar mission delays as LQR-O.

Thus, *DeLorean*'s attack diagnosis guided attack recovery prevents unnecessary mission delays while recovering from multi-sensor SDAs.

6.4 Attack diagnosis and Recovery in Real RVs

We also evaluate *DeLorean* on the four real RVs under SDAs targeting different numbers of sensors. Table 7 shows *DeLorean*'s diagnosis and recovery outcomes. We find that *DeLorean*'s diagnosis achieves 100% TP rate when the SDA targets up to 2 sensors simultaneously. However, its TP rate drops to between 80% and 90% when the SDA targets 3 or more sensors. On average, *DeLorean*'s attack diagnosis TP rate is between 92% to 98% across all RVs. We also find that *DeLorean*'s diagnosis FP rate was between 2% and 6% across all RVs (not presented due to space constraints). These results are comparable to those on the simulated RVs (Section 6.1).

Table 7: *DeLorean*'s attack diagnosis and attack recovery in real RVs. All values shown in percentage.

# of sensors targeted	Pixhawk		Tarrort		Sky-viper		Aion R1	
	TP	MS	TP	MS	TP	MS	TP	MS
1	100	100	100	100	100	100	100	100
2	100	100	100	100	100	100	100	100
3	90	100	100	100	80	100	80	100
4	90	80	90	90	80	80	90	80
5	100	80	100	80	100	80	100	80
Average	96	92	98	94	92	92	94	92

We find that *DeLorean*'s average mission success rate for SDAs targeting upto $n - 1$ of the RV's sensors is 95.62%. Furthermore, *DeLorean* successfully recovered RVs in 100% of the cases when the SDA targets up to 3 sensors simultaneously. However, its mission success rate drops to 80% when SDAs target all the 5 sensors simultaneously. *DeLorean* achieves 92.5% average mission success rate across RVs. Furthermore, we observed no crashes in any of the real RV mission. Finally, even for the failed missions, the deviation from the target was very small (15.6m on average).

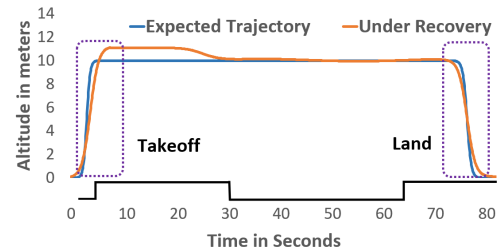


Figure 9: *DeLorean*'s recovery in the Pixhawk drone under SDAs. Bottom graph shows when the SDA is launched.

Figure 9 shows *DeLorean*'s recovery on the real Pixhawk drone when SDAs targeted GPS and accelerometer sensors simultaneously. This experiment closely resembles the one discussed in Section 3.2. We deliberately target 2 out of 5 sensors to compare with LQR-O's recovery discussed in Section 3.2 and *DeLorean*'s targeted recovery. In this mission, the drone should attain an elevation of 10m and navigate in a straight line for 70s, and land when it reaches the destination. Two instances of SDAs were launched: (i) during the takeoff from 5s to 30s, (ii) during landing from 65s to 85s. Note that,

in a similar mission, shown earlier in Figure 2, LQR-O incurred an RMSE of 20.66, a mission delay of 18.75%, and resulted in a mission failure with the drone landing 15m off the target destination.

In contrast, when *DeLorean* is deployed in the Pixhawk drone, it achieved RMSD of 4.21, caused only 2.5% mission delay, and it completed the mission successfully landing the drone at the destination. As shown in Figure 9, *DeLorean* limited deviations from the expected trajectory to 1.5m under the first SDA during takeoff. *DeLorean* maneuvered the drone without incurring any additional delays and landed it safely under the second SDA. Therefore, *DeLorean*'s diagnosis and targeted recovery successfully navigated the drone toward its set target and completed the mission successfully.

6.5 Recovery under Stealthy Attacks

Recall that *DeLorean* sets a historic states recording window large enough that a stealthy attack that injects persistent bias can be detected in one sliding window using CUSUM [22]. An attacker who is aware of this design can launch adaptive stealthy attacks by introducing variations in the bias. The attacker's goal is to prolong the stealthy attack duration while evading detection, corrupt the *DeLorean*'s recorded historic states, and consequently, affect *DeLorean*'s recovery process. We perform experiments on ArduCopter to evaluate *DeLorean* under three adaptive stealthy attacks. Instead of persistent bias, these adaptive attacks inject: (A1) random bias, (A2) gradually increasing bias, and (A3) intermittent bias.

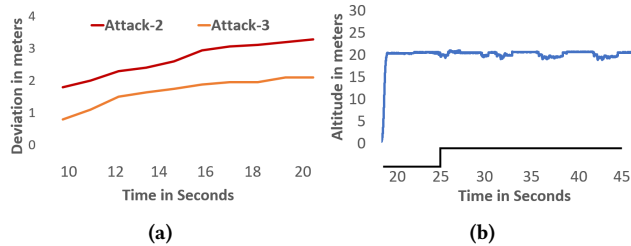


Figure 10: *DeLorean* recovery in ArduCopter under stealthy attacks. (a) Corruptions in recorded states due to stealthy attacks, (b) Recovery under stealthy attacks.

In the first experiment, we launched attack A1 following the drone takeoff, and we targeted all the sensors simultaneously. We injected random bias causing deviations between 0-5m in the RV's trajectory. We found that this attack was detected within one sliding window. Thus, attack-A1 failed to corrupt the *DeLorean*'s historic states, and consequently, *DeLorean* performed a successful recovery.

In the second experiment, we launched attack A2 starting at $t=10s$. This attack remained undetected in the initial sliding window and caused a total deviation of 3.28m from the drone's original path (Figure 10a). Thus, attack A2 successfully corrupted *DeLorean*'s historic states. As no alarm was raised by the attack detector, *DeLorean* recorded corrupted historic states. At $t=25s$ the attack was detected and recovery activated. As shown in Figure 10b, *DeLorean* was able to successfully recover the drone, maintaining its altitude at 20m despite the corruption in the historic states. This is because the corruption in historic states due to attack A2 is negligible, and hence it does not disrupt *DeLorean*'s recovery control actions.

Finally, we evaluated *DeLorean* under attack A3. We launched the attack intermittently following the RV's takeoff. This attack also managed to evade detection but resulted in a 2.1m total deviation from the RV's original path. Consequently, *DeLorean* recorded the corrupted historic states similar to the A2 scenario. We find that *DeLorean* successfully recovered the RV as the historic states corruptions exhibited negligible impact on the recovery process.

Thus, *DeLorean* ensures timely detection of a stealthy attack within one sliding window, thereby ensuring no corruption of the recovery process. Furthermore, *DeLorean*'s robustness to the historic states' corruptions under adaptive stealthy attacks ensures successful recovery.

6.6 Overheads

Table 3 shows the overheads incurred by *DeLorean* on the real RVs. The CPU overhead varies from 5.5% to 9.2%, with an average of 7.5% across the four RVs. This is slightly higher than the CPU overhead incurred by SSR and PID-Piper, which are 6.9% and 6.35% respectively (on similar RV platforms). However, because LQR-O does not report CPU overhead, we estimate its overhead based on *DeLorean*'s overhead. As LQR-O does not perform any diagnosis unlike *DeLorean*, we subtract the cost of diagnosis from *DeLorean*'s overhead, which comes to an average 7% across the RVs.

Furthermore, *DeLorean*'s memory overhead is between 0.45 MB and 0.56 MB across the different RVs. This accounts for less than 3% overhead, as the memory available on the real RVs is over 20 MB.

Finally, under attacks, *DeLorean* incurs battery overheads between 14.4% and 22% across RVs (18.87% on average). This overhead is a result of recovery control actions and mission delays, causing the motors to remain operational for an extended period. In comparison, LQR-O incurs significantly higher battery overhead as it incurs 2.5X higher mission delays than *DeLorean*. Note that we did not measure the battery overheads for PID-Piper and SSR as they do not recover from most SDAs.

7 CONCLUSION

We presented *DeLorean*, a unified framework for attack detection, diagnosis, and recovery from multi-sensor SDAs in RVs. We proposed a factor graphs based attack diagnosis method that inspects the attack induced errors in the RV's physical states and performs causal analysis to identify the sensors targeted by SDAs. *DeLorean* then isolates those sensors from RV's feedback control loop to prevent erroneous control actions. *DeLorean* integrates existing attack detection and recovery techniques with our proposed attack diagnosis technique to provide targeted attack recovery in RVs. We evaluate *DeLorean* on four real and two simulated RVs. We find that *DeLorean* (1) recovers the RVs from SDAs, and achieves mission success in 93% of the cases, (2) minimizes mission disruptions during recovery by performing diagnosis guided targeted recovery, and (3) achieves mission success even against stealthy attacks, and (4) incurs modest performance, memory, and battery overheads.

ACKNOWLEDGEMENTS

This work was partially supported by the Natural Sciences and Engineering Research Council of Canada (NSERC), and a Four Year Fellowship from UBC. We thank the reviewers of AsiaCCS'24 and our shepherd Dr. Jairo Giraldo for their helpful comments.

REFERENCES

- [1] [n. d.]. AGRAS T16 - Agriculture Spraying Drone. <https://www.dji.com/ca/t16>.
- [2] [n. d.]. Aion R1 ArduPilot Edition. <https://docs.aionrobotics.com/en/latest/r1-ugv.html>.
- [3] [n. d.]. Amazon Robotics. <https://robots.ieee.org/robots/kiva/>.
- [4] [n. d.]. Ardupilot - Software in the Loop. <http://ardupilot.org/dev/docs/sitl-simulator-software-in-the-loop.html>.
- [5] [n. d.]. Beaufort Wind Scale. <https://www.weather.gov/ml/beaufort>.
- [6] [n. d.]. A downed drone highlights a vulnerable technology. <https://www.washingtonpost.com/politics/2023/03/16/downed-us-drone-points-cyber-vulnerabilities/>.
- [7] [n. d.]. Gazebo robot simulation. <http://gazebosim.org/>.
- [8] [n. d.]. PID-Piper Code. <https://github.com/DependableSystemsLab/pid-piper>.
- [9] [n. d.]. Sky Viper Journey Drone. <https://sky-viper.com/journey/>.
- [10] [n. d.]. System Identification Overview. <https://www.mathworks.com/help/ident/g/about-system-identification.html>.
- [11] [n. d.]. Tarot 650 v2 Drone. <https://uavsystemsinternational.com/products/tarot-650-ready-to-fly-drone>.
- [12] [n. d.]. u-blox M8 concurrent GNSS modules. <https://www.u-blox.com/en/product/neo-m8-series>.
- [13] Chuadhry Mujeeb Ahmed, Jianying Zhou, and Aditya P. Mathur. 2018. Noise Matters: Using Sensor and Process Noise Fingerprint to Detect Stealthy Cyber Attacks and Authenticate Sensors in CPS. In *Proceedings of the 34th Annual Computer Security Applications Conference* (San Juan, PR, USA) (ACSAC '18). ACM, New York, NY, USA, 566–581. <https://doi.org/10.1145/3274694.3274748>.
- [14] Nathan Burow, Scott A. Carr, Joseph Nash, Per Larsen, Michael Franz, Stefan Brunthaler, and Mathias Payer. 2017. Control-Flow Integrity: Precision, Security, and Performance. *ACM Comput. Surv.* 50, 1, Article 16 (April 2017), 33 pages. <https://doi.org/10.1145/3054924>.
- [15] Phuong Cao, Eric Badger, Zbigniew Kalbarczyk, Ravishankar Iyer, and Adam Slagell. 2015. Preemptive Intrusion Detection: Theoretical Framework and Real-World Measurements. In *Proceedings of the 2015 Symposium and Bootcamp on the Science of Security* (Urbana, Illinois) (HotSoS '15). Association for Computing Machinery, New York, NY, USA, Article 5, 12 pages. <https://doi.org/10.1145/2746194.2746199>.
- [16] Yulong Cao, Ningfei Wang, Chaowei Xiao, Dawei Yang, Jin Fang, Ruigang Yang, Qi Alfred Chen, Mingyan Liu, and Bo Li. 2021. Invisibile for both Camera and LiDAR: Security of Multi-Sensor Fusion based Perception in Autonomous Driving Under Physical-World Attacks. *2021 IEEE Symposium on Security and Privacy (SP)* (May 2021). <https://doi.org/10.1109/sp40001.2021.00076>.
- [17] Y. Chen, C. M. Poskitt, and J. Sun. 2018. Learning from Mutants: Using Code Mutation to Learn and Monitor Invariants of a Cyber-Physical System. In *2018 IEEE Symposium on Security and Privacy (SP)*. IEEE Computer Society, Los Alamitos, CA, USA, 648–660. <https://doi.org/10.1109/SP.2018.00016>.
- [18] Hongjun Choi, Sayali Kate, Youssa Aafer, Xiangyu Zhang, and Dongyan Xu. 2020. Software-based Realtime Recovery from Sensor Attacks on Robotic Vehicles. In *23rd International Symposium on Research in Attacks, Intrusions and Defenses (RAID 2020)*. USENIX Association, San Sebastian, 349–364.
- [19] Hongjun Choi, Wen-Chuan Lee, Youssa Aafer, Fan Fei, Zhan Tu, Xiangyu Zhang, Dongyan Xu, and Xinyan Deng. 2018. Detecting Attacks Against Robotic Vehicles: A Control Invariant Approach. In *Proceedings of the 2018 ACM SIGSAC Conference on Computer and Communications Security* (Toronto, Canada) (CCS '18). ACM, New York, NY, USA, 801–816. <https://doi.org/10.1145/3243734.3243752>.
- [20] Pritam Dash, Mehdi Karimibiuki, and Karthik Pattabiraman. 2019. Out of Control: Stealthy Attacks Against Robotic Vehicles Protected by Control-based Techniques. In *Proceedings of the 35th Annual Computer Security Applications Conference* (San Juan, Puerto Rico) (ACSAC '19). ACM, New York, NY, USA, 660–672. <https://doi.org/10.1145/3359789.3359847>.
- [21] Pritam Dash, Mehdi Karimibiuki, and Karthik Pattabiraman. 2021. Stealthy Attacks against Robotic Vehicles Protected by Control-Based Intrusion Detection Techniques. *Digital Threats* 2, 1, Article 7 (jan 2021), 25 pages. <https://doi.org/10.1145/3419474>.
- [22] Pritam Dash, Guanpeng Li, Zitao Chen, Mehdi Karimibiuki, and Karthik Pattabiraman. 2021. PID-Piper: Recovering Robotic Vehicles from Physical Attacks. In *2021 51st Annual IEEE/IFIP International Conference on Dependable Systems and Networks (DSN)*. 26–38. <https://doi.org/10.1109/DSN48987.2021.00020>.
- [23] Drew Davidson, Hao Wu, Rob Jellinek, Vikas Singh, and Thomas Ristenpart. 2016. Controlling UAVs with Sensor Input Spoofing Attacks. In *10th USENIX Workshop on Offensive Technologies (WOOT 16)*. USENIX Association, Austin, TX. <https://www.usenix.org/conference/woot16/workshop-program/presentation/davidson>.
- [24] Gene F. Franklin, J. David Powell, and Abbas Emami-Naeini. 2018. *Feedback Control of Dynamic Systems (8th Edition) (What's New in Engineering)*. Pearson.
- [25] M.R. Gauthama Raman, Wenjie Dong, and Aditya Mathur. 2020. Deep autoencoders as anomaly detectors: Method and case study in a distributed water treatment plant. *Computers and Security* 99 (2020), 102055. <https://doi.org/10.1016/j.cose.2020.102055>.
- [26] David Hambling. 2021. UK ship hit by GPS spoof. *New Scientist* 250, 3341 (2021), 17. [https://doi.org/10.1016/S0262-4079\(21\)01131-3](https://doi.org/10.1016/S0262-4079(21)01131-3).
- [27] Kim Hartmann and Christoph Steup. 2013. The vulnerability of UAVs to cyber attacks—An approach to the risk assessment. In *2013 5th international conference on cyber conflict (CYCON 2013)*. IEEE, 1–23.
- [28] Andrew J. Hawkins. [n. d.]. *UPS will use drones to deliver medical supplies in North Carolina*. Retrieved May 24, 2019 from <https://www.theverge.com/2019/3/26/18282291/ups-drone-delivery-hospital-nc-matternet>.
- [29] Todd E. Humphreys. 2008. Assessing the Spoofing Threat: Development of a Portable GPS Civilian Spoofers. In *In Proceedings of the Institute of Navigation GNSS (ION GNSS)*.
- [30] Arslan Khan, Hyungsub Kim, Byoungyoung Lee, Dongyan Xu, Antonio Bianchi, and Dave Jing Tian. 2021. M2MON: Building an MMIO-based Security Reference Monitor for Unmanned Vehicles. In *30th {USENIX} Security Symposium ({USENIX} Security 21)*.
- [31] Fanxin Kong, Meng Xu, James Weimer, Oleg Sokolsky, and Insup Lee. 2018. Cyber-Physical System Checkpointing and Recovery. In *2018 ACM/IEEE 9th International Conference on Cyber-Physical Systems (ICCP)*. 22–31. <https://doi.org/10.1109/ICCP.2018.00011>.
- [32] Jason Kong, Mark Pfeiffer, Georg Schildbach, and Francesco Borrelli. 2015. Kinematic and dynamic vehicle models for autonomous driving control design. In *2015 IEEE Intelligent Vehicles Symposium (IV)*. 1094–1099. <https://doi.org/10.1109/IVS.2015.7225830>.
- [33] Yucong Lin and Srikanth Saripalli. 2015. Sense and avoid for unmanned aerial vehicles using ADS-B. In *2015 IEEE International Conference on Robotics and Automation (ICRA)*. IEEE, 6402–6407.
- [34] L. Ljung. 1979. Asymptotic behavior of the extended Kalman filter as a parameter estimator for linear systems. *IEEE Trans. Automat. Control* 24, 1 (February 1979), 36–50. <https://doi.org/10.1109/TAC.1979.1101943>.
- [35] Lorenz Meier, Petri Tanskanen, Friedrich Fraundorfer, and Marc Pollefeys. 2011. Pixhawk: A system for autonomous flight using onboard computer vision. In *2011 IEEE International Conference on Robotics and Automation*. IEEE, 2992–2997.
- [36] Shoeni Nashimoto, Daisuke Suzuki, Takeshi Sugawara, and Kazuo Sakiyama. 2018. Sensor CON-Fusion: Defeating Kalman Filter in Signal Injection Attack. In *Proceedings of the 2018 on Asia Conference on Computer and Communications Security (Incheon, Republic of Korea) (ASIACCS '18)*. Association for Computing Machinery, New York, NY, USA, 511–524. <https://doi.org/10.1145/3196494.3196506>.
- [37] Juhwan Noh, Yujin Kwon, Yunmok Son, Hocheol Shin, Dohyun Kim, Jaeyeong Choi, and Yongdae Kim. 2019. Tractor beam: Safe-hijacking of consumer drones with adaptive GPS spoofing. *ACM Transactions on Privacy and Security (TOPS)* 2, 2 (2019), 1–26.
- [38] Raul Quinonez, Jairo Giraldo, Luis Salazar, Erick Bauman, Alvaro Cardenas, and Zhiqiang Lin. 2020. SAVIOR: Securing Autonomous Vehicles with Robust Physical Invariants. In *29th USENIX Security Symposium (USENIX Security 20)*. USENIX Association, Boston, MA.
- [39] Clemens Reimann, Peter Filzmoser, and Robert G. Garrett. 2005. Background and threshold: critical comparison of methods of determination. *Science of The Total Environment* 346, 1 (2005), 1–16. <https://doi.org/10.1016/j.scitotenv.2004.11.023>.
- [40] Brent A. Renfro, Miquela Stein, Nicholas Boeker, Emery Reed, and Eduardo Villalba. [n. d.]. An Analysis of Global Positioning System (GPS) Standard Positioning Service (SPS) Performance for 2018.
- [41] Yunmok Son, Hocheol Shin, Dongkwan Kim, Youngseok Park, Juhwan Noh, Kibum Choi, Jungwoo Choi, and Yongdae Kim. 2015. Rocking Drones with Intentional Sound Noise on Gyroscopic Sensors. In *24th USENIX Security Symposium (USENIX Security 15)*. USENIX Association, Washington, D.C., 881–896.
- [42] Nils Ole Tippenhauer, Christina Pöpper, Kasper Bonne Rasmussen, and Srđjan Capkun. 2011. On the Requirements for Successful GPS Spoofing Attacks. In *Proceedings of the 18th ACM Conference on Computer and Communications Security* (Chicago, Illinois, USA) (CCS '11). ACM, New York, NY, USA, 75–86. <https://doi.org/10.1145/2046707.2046719>.
- [43] Yazhou Tu, Zhiqiang Lin, Insup Lee, and Xiali Hei. 2018. Injected and Delivered: Fabricating Implicit Control over Actuation Systems by Spoofing Inertial Sensors. In *27th USENIX Security Symposium (USENIX Security 18)*. USENIX Association, Baltimore, MD, 1545–1562. <https://www.usenix.org/conference/usenixsecurity18/presentation/tu>.
- [44] Nian Xue, Liang Niu, Xianbin Hong, Zhen Li, Larissa Hoffaeller, and Christina Pöpper. 2020. DeepSIM: GPS Spoofing Detection on UAVs Using Satellite Imagery Matching. In *Annual Computer Security Applications Conference* (Austin, USA) (ACSAC '20). Association for Computing Machinery, New York, NY, USA, 304–319. <https://doi.org/10.1145/3427228.3427254>.
- [45] Lin Zhang, Xin Chen, Fanxin Kong, and Alvaro A Cardenas. 2020. Real-time attack-recovery for cyber-physical systems using linear approximations. In *2020 IEEE Real-Time Systems Symposium (RTSS)*. IEEE, 205–217.
- [46] Lin Zhang, Pengyuan Lu, Fanxin Kong, Xin Chen, Oleg Sokolsky, and Insup Lee. 2021. Real-Time Attack-Recovery for Cyber-Physical Systems Using Linear-Quadratic Regulator. *ACM Trans. Embed. Comput. Syst.* 20, 5s, Article 79 (sep 2021), 24 pages. <https://doi.org/10.1145/3477010>.

A RESEARCH METHODS

A.1 Joint Probability and Factor Graphs

The joint probability of variables x_1, \dots, x_n is described as $P(x_1, \dots, x_n)$. Causal inference of an event given the observed variable is calculated as: $y = \operatorname{argmax} P(y|x_1, \dots, x_{n-1})$, which can be further expanded as the following.

$$P(y|x_1, \dots, x_{n-1}) = \frac{P(x_1, \dots, x_{n-1})}{\sum_v P(x_1, \dots, x_{n-1}, y = v)} \quad (7)$$

Inference on a joint probability distribution $P(x_1, \dots, x_n)$ requires 2^n storage for events with a binary outcome (e.g., malicious, benign), which is computationally expensive as well.

Factor graphs can be used to overcome this problem. A factor graph (FG) is a probabilistic graphical model that allows expressing joint probability as a product of smaller local functions [15]. Figure 11 shows an example. There are two types of nodes in a FG namely variables (x_1, x_2, x_3) and factor functions (f_1, f_2, f_3). Variables are used to quantitatively describe an event. A factor function is used to express relationships among variables.

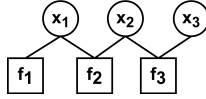


Figure 11: An example of factor graph

Let's take Figure 11 as an example to understand how to calculate conditional probability using a factor graph. The variables $x_1, x_2, x_3 \in X$, and y is the outcome. $P(x_1, x_2, x_3)$ can be factored as a product of f_1, f_2, f_3 .

$$P(x_1, x_2, x_3) = f_1(x_1), f_2(x_1, x_2), f_3(x_2, x_3) \quad (8)$$

Thus, the conditional probability of an event given the observed variables is calculated as:

$$P(y|x_1, x_2, x_3) = \prod_{f \in F} f(x) \quad (9)$$

Using sum-product algorithm, the marginal is defined as $P(x) = \sum_{x \in X} P(X)$. Thus, the conditional probability of an event given the observed variables is calculated as the following.

$$P(y|x_1, x_2, x_3) = \sum f(x) \quad (10)$$

A.2 Extended Kalman Filter Implementation

Extended Kalman Filter (EKF) is a version of Kalman Filter that is used to estimate the state dynamics of a non-linear system. EKF consists of two steps: estimation and correction. State estimation is done using a non-linear function of the system $f(\cdot)$. The following equation shows EKF's state estimation, where x_t is the state estimated in the previous time step, u_t is the actuator command.

$$x_{t+1} = f(x_t, u_t) \quad (11)$$

Equation 12 shows how EKF state correction is done using the available sensor measurements. y_t is the sensor measurement, $h(\hat{x}_{t|t-1})$ are EKF computed states in the previous time step, and K

is the Kalman Gain. Note that the Kalman Gain K is calculated using Jacobian of transition and observation matrices and the sensor noise covariance matrix.

$$\hat{x}_{t+1} = f(x_t, u_t) + K_t(y_t - h(\hat{x}_{t|t-1})) \quad (12)$$

We use non-linear system dynamics equations of RVs as models in our EKF estimator and for each RV we learn the model parameters (unknown coefficients) using system identification [10]. We collect a dataset of control actions and sensor measurements for each of our subject RVs. For example, we run missions capturing sensor readings and control signals to the rotors in various modes of operation of a drone - takeoff, loiter, auto, circle, and land.

A quadcopter's state vector represents its position (x, y, z), velocity (v_x, v_y, v_z), angular orientation (ϕ, θ, ψ), and angular speed ($\omega_\phi, \omega_\theta, \omega_\psi$). The following equations show the quadcopter dynamics [38]. U_t is the thrust force, U_ϕ, U_θ, U_ψ are control commands for rotors (roll, pitch, yaw), I_x, I_y, I_z are moments of inertia in x, y, z axis respectively, g is gravity, and m is the mass.

$$\begin{aligned} \dot{x} &= v_x \\ \dot{y} &= v_y \\ \dot{z} &= v_z \\ \dot{v}_x &= \frac{U_t}{m} (\cos \phi \sin \theta \cos \psi + \sin \phi \sin \psi) \\ \dot{v}_y &= \frac{U_t}{m} (\cos \phi \sin \theta \sin \psi - \sin \phi \cos \psi) \\ \dot{v}_z &= \frac{U_t}{m} \cos \phi \cos \theta - g \\ \dot{\phi} &= \omega_\phi \\ \dot{\theta} &= \omega_\theta \\ \dot{\psi} &= \omega_\psi \\ \dot{\omega}_\phi &= \frac{U_\phi}{I_x} + \dot{\theta} \dot{\psi} \left(\frac{I_y - I_z}{I_x} \right) \\ \dot{\omega}_\theta &= \frac{U_\theta}{I_y} + \dot{\phi} \dot{\psi} \left(\frac{I_z - I_x}{I_y} \right) \\ \dot{\omega}_\psi &= \frac{U_\psi}{I_z} + \dot{\phi} \dot{\theta} \left(\frac{I_x - I_y}{I_z} \right) \end{aligned}$$

The following equations show ground rover dynamics [32], where β is the slip angle - measures sideways movement of wheels, δ is the steering angle, l_f is the distance between center of mass and front axle, l_r is the distance between center of mass and rear axle.

$$\begin{aligned} \beta &= \tan^{-1} \left(\frac{l_r}{l_f + l_r} \tan(\delta) \right) \\ \dot{x} &= v \cos(\psi + \beta) \\ \dot{y} &= v \sin(\psi + \beta) \\ \dot{\psi} &= \frac{v}{l_r} \sin(\beta) \\ \dot{v} &= a \end{aligned}$$

A.3 Algorithm

Algorithm 1 shows *DeLorean*'s algorithm for attack diagnosis and recovery. In the absence of attacks (based on the attack detector's response), *DeLorean* records the physical states associated with all the on-board sensors (Lines 7-15) in a sliding window. Once the attack detector raises an alert, *DeLorean* activates recovery mode (Line 17). First, it stops recording, and prepares the most recent safe *HS* for recovery. Then, it activates the diagnosis procedure (Line 21). The attack diagnosis module determines the sensors under attack, if any, using FGs (Line 28-34). Once the targeted sensors are determined, *DeLorean* uses the historic states for the compromised sensors and current state estimates from uncompromised sensors to reconstruct RV's states (Line 23), effectively representing the RV's states at the time when attack recovery was activated. This ensures that the inputs to the recovery technique remain untainted by SDA manipulations, enabling the recovery technique to derive safe control actions. Once the attack subsides (based on the attack detector's response), the recovery mode is turned off.

Algorithm 1 Algorithm for Attack Diagnosis and Recovery

```

1:  $w \leftarrow$  historic state recording window
2:  $S \leftarrow$  historic physical states used for recovery
3:  $x_r \leftarrow$  physical states corresponding to targeted sensors
4:  $x_s \leftarrow$  physical states corresponding to uncompromised sensors
5: procedure ATTACKRECOVERY
6:    $alert \leftarrow$  AttackDetector()
7:   while !mission_end do
8:     if !alert then                                ▶ recording historic states
9:        $recovery\_mode \leftarrow$  false
10:      if  $t_w < t_{w+1}$  then
11:         $record \leftarrow$  true
12:         $w_i[.] \leftarrow$   $x(t)$ 
13:      else
14:         $delete\ w_{i-1}$ 
15:         $t_w = t_{w+1}$ 
16:      end if
17:    else                                          ▶ recovery activated
18:       $recovery\_mode \leftarrow$  true
19:       $record \leftarrow$  False
20:       $HS = w_{i-1}$ 
21:       $targetedSensors \leftarrow$  Diagnosis()
22:       $x_r \leftarrow$  estimateStates(HS[.])
23:       $X_r[.] \leftarrow$  stateReconstruction( $x_r, x_s$ )  ▶ state reconstruction
24:    end if
25:  end while
26: end procedure
27: procedure DIAGNOSIS
28:   while !mission_end  $\forall$  sensors do
29:      $e = |(e_t) - (e_{t-1})|$ 
30:      $s_t \leftarrow$  argmaxP( $s_t|e$ )                    ▶ most probable outcome
31:     if  $s_t = 1$  then
32:       return malicious                              ▶ targeted sensors
33:     end if
34:   end while
35: end procedure

```

A.4 Mission Types

We run a diverse set of missions to derive the experimental parameters and for our experiments. Table 8 shows the details.

A.5 Metrics

Normalized RMSD As minor attitude deviations are expected in RV missions even in the same trajectory due to variations in control signals and computations in RV's feedback control loop.

Table 8: Mission paths used in evaluating *DeLorean*. S: Straight line, MW: Multiple waypoints, C: Circular, and Three different polygonal paths P1, P2, and P3

Mission Paths	S	MW	C	P1	P2	P3	Total
Number of missions	70	70	50	50	50	50	340

To ensure that these minor deviations are accounted for in our recovery stability metric, we introduce a normalization technique for the RMSD values. This normalization approach transforms the RMSD values (calculation shown in Equation 5) into a standardized range between 0 and 1 as follows:

$$Normaized\ RMSD = \frac{RMSD - min\ RMSD}{max\ RMSD - min\ RMSD} \quad (13)$$

Where *min RMSD* and *max RMSD* are minimum and maximum RMSD values among recovery activated missions.

Normalized Mission Delay As minor variations in mission completion times can occur even on the same trajectory, we normalize the mission delay using a baseline mission completion time $T_{baseline}$ as the reference point for mission completion time for an RV on a given trajectory. $T_{baseline}$ is derived using min-max approach as shown below. Where $T_{baseline}$ is the average of the minimum and maximum mission completion times in attack-free missions.

$$T_{baseline} = \frac{T_{min} + T_{max}}{2} \quad (14)$$